*Article*

# Improving Zinc-Ion Batteries' Performance: The Role of Nitrogen Doping in $V_2O_3$/C Cathodes

**He Lin *** , **Huanhuan Cheng and Yu Zhang**

A State Key Laboratory of Chemistry and Utilization of Carbon Based Energy Resources, School of Chemistry, Xinjiang University, Urumqi 830017, China; linhe80@gmail.com (H.C.); cnuo017@gmail.com (Y.Z.)
* Correspondence: helin@xju.edu.cn; Tel.: +86-180-4090-9207

**Abstract:** This study presents the synthesis and electrochemical evaluation of nitrogen-doped vanadium oxide ($N-V_2O_3$/C) as a cathode material for aqueous zinc-ion batteries (AZIBs), using a hydrothermal method. Compared to undoped $V_2O_3$/C, $N-V_2O_3$/C exhibits enhanced electrical conductivity, capacity, and electrochemical kinetics, attributed to the incorporation of pyridinic and pyrrolic nitrogen. The initial charge–discharge cycles indicate phase transitions to amorphous vanadium oxides, enhancing conductivity. $N-V_2O_3$/C shows a high specific capacity of 168.4 mAh g$^{-1}$ at 10 A g$^{-1}$ and remarkable reversibility, highlighted by the transient existence of intermediate species during cycling. Optimal electrochemical performance is achieved with a vanadium-to-nitrogen molar ratio of 2:3, indicating the significant impact of the nitrogen doping concentration on the material's efficiency. This work underscores the potential of $N-V_2O_3$/C as a superior cathode material for AZIBs.

**Keywords:** nitrogen-doped vanadium oxide; cathode; aqueous zinc-ion batteries; phase transition

## 1. Introduction

Amid growing concerns over climate change and environmental degradation, the exploration and development of renewable energy sources, including solar and wind energy, have garnered substantial global interest [1,2]. The efficient harnessing of these renewable resources necessitates advancements in energy storage technologies that not only offer high conversion efficiencies but also ensure elevated safety standards. Lithium-ion batteries (LIBs) have emerged as a prominent solution for high-efficiency energy storage, gaining widespread adoption across various portable electronic markets [3,4]. Nonetheless, the scalability of LIBs is hampered by significant drawbacks, such as safety concerns, the high cost of production, and the scarcity of lithium reserves beneath the Earth's surface [5].

In this context, aqueous zinc-ion batteries (AZIBs) have been identified as potent alternatives for large-scale energy storage applications, thanks to their myriad benefits [6,7]. These include enhanced safety, reduced manufacturing costs, straightforward production processes, and superior capacity and power density metrics. The global abundance of zinc, coupled with its ease of extraction and compatibility with aqueous electrolytes, further accentuates the appeal of AZIBs. Moreover, the majority of AZIB systems utilize neutral or mildly acidic aqueous solutions, offering a safer and more environmentally friendly alternative to the organic electrolytes used in traditional battery technologies [8–10]. Given these substantial advantages, AZIBs are increasingly viewed as viable successors to LIBs in the quest for sustainable and safe large-scale energy storage solutions [11,12].

The cathode plays a critical role in dictating the electrochemical performance of batteries, particularly in the domain of aqueous zinc-ion batteries (AZIBs) [13–15]. Therefore, the development of high-performance cathode materials is crucial for the effective deployment of AZIB technology. Vanadium-based compounds, a prevalent category of cathode materials for AZIBs, offer a wide array of coordination polyhedra and crystal structures

attributed to the multiple oxidation states of vanadium ($V^{2+}$, $V^{3+}$, $V^{4+}$, and $V^{5+}$) [16]. This variability facilitates high theoretical capacities. Notably, compounds such as $V_2O_5$ [17–19], $VO_2$ [20,21], $VS_4$ [22], $VOPO_4$ [23], $MnV_2O_4$ [24], and $V_6O_{13}$ [25], and $V_2O_3$ [26–28] have been extensively explored and reported.

Despite their potential, vanadium-based materials are hindered by inadequate conductivity and sluggish kinetic responses. To mitigate these limitations, integration with carbon materials has been pursued to amplify the electrochemical attributes of vanadium-based compositions [29]. Notably, composites of vanadium oxides and carbon nanomaterials are distinguished by their enhanced electrical conductivity and expanded ion diffusion pathways, which contribute to their pronounced reversibility. Furthermore, the inherent challenges of low wettability and reactivity in pristine carbon materials necessitate their functionalization or doping with heteroatoms (e.g., N, P, S) to foster improved performance characteristics. Within the scope of heteroatom-doped carbonaceous nanomaterials engineering, N doping emerges as a pivotal technique for augmenting surface energy and reactivity through charge polarization enhancement, thereby elevating the efficacy of devices dedicated to electrochemical energy storage or conversion [30]. Despite these advancements, the domain of heteroatom doping within vanadium-based materials remains underexplored, indicating a significant avenue for future research.

Expanding upon prior analyses, this study integrates heteroatoms into carbon matrices to augment the electrochemical attributes of vanadium oxides. Utilizing a hydrothermal synthesis approach, we engineered nitrogen-doped, carbon-coated $V_2O_3$ (denoted as $N-V_2O_3/C$) and assessed its electrochemical prowess as a cathode in AZIBs, juxtaposed against its undoped counterpart, $V_2O_3/C$. Observations post the inaugural charge–discharge cycle indicated a phase transition in both electrode variants, culminating in the formation of amorphous vanadium oxides.

Analytical methods, including X-ray photoelectron spectroscopy (XPS), disclosed an elevation in the $V^{5+}$ ratio subsequent to the initial charging event, thereby establishing a cornerstone for enhanced electrochemical performance. Electrochemical evaluations demonstrated that nitrogen doping, manifesting through the presence of pyridinic and pyrrolic nitrogen species, significantly uplifted the cyclic capacity and electron diffusion rates. Further scrutiny into the zinc storage mechanism elucidated the emergence and subsequent dissolution of novel phases throughout the charging and discharging sequences, signaling pronounced reversibility. Additionally, the study delved into the quantification of nitrogen doping levels, determining that an optimal electrochemical response was realized at a vanadium-to-nitrogen source molar ratio of 2:3.

## 2. Results and Discussion

### 2.1. Material Characterization

In contrast to the commonly utilized nitrogen source urea, the thiourea molecule features a less stable C=S double bond and amino $p-\pi$-conjugated bonds, thereby facilitating a more ready detachment of nitrogen. Leveraging this property, thiourea was chosen as the nitrogen precursor, vanadium acetylacetonate as the vanadium source, and glucose as the carbon scaffold for the hydrothermal synthesis of $N-V_2O_3/C$. The structural paradigm of $V_2O_3$, depicted in Figure 1a, showcases a trigonal crystal system (space group $R\bar{3}c$) characterized by a three-dimensional lattice conducive to electron mobility within vanadium−vanadium (V−V) chain frameworks, thus exhibiting metallic properties. Vanadium atoms are strategically positioned within two-thirds of the octahedral sites formed by oxygen atoms. This arrangement is further complemented by the connectivity of two [$VO_6$] octahedra with their neighboring atoms through shared corners, faces, and edges, culminating in a tunnel-like three-dimensional matrix. Such a configuration is optimally designed to support the facile insertion and extraction of metal ions, pivotal for the material's electrochemical performance.
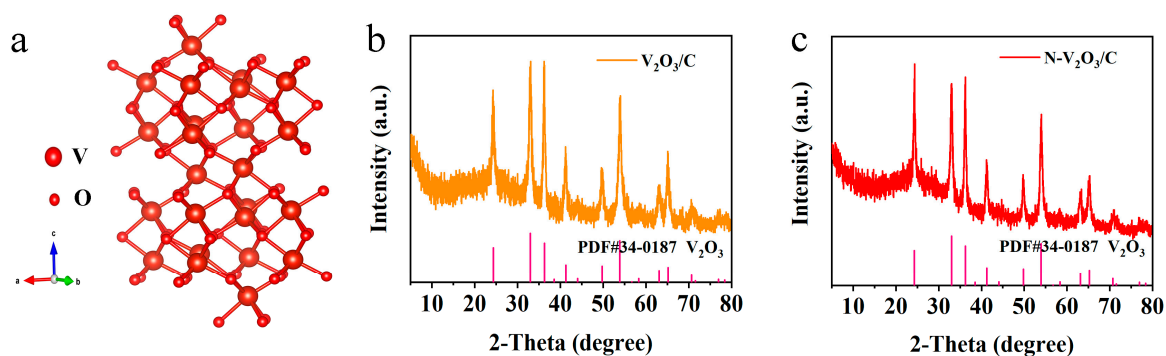
**Figure 1.** (**a**) Structure of $V_2O_3$; XRD patterns of (**b**) $V_2O_3/C$ and (**c**) $N-V_2O_3/C$.

The X-ray diffraction (XRD) patterns confirm the successful synthesis of the target product. Within the $V_2O_3/C$ composite, the lack of distinctive carbon peaks indicates the carbon exists in an amorphous state, thereby not detracting from the crystalline integrity of $V_2O_3$, as demonstrated in Figure 1b. Moreover, the incorporation of a nitrogen-doped carbon coating within the $N-V_2O_3/C$ composite does not impede the crystallization of $V_2O_3$, corroborated by the data presented in Figure 1c.

The SEM analysis of the synthesized samples elucidates a significant morphological transition attributed to the doping of N into the system. Initially, the $V_2O_3/C$ composite showcases nanoparticles with irregular geometries, as evidenced by the SEM images presented in Figure 2a–c at various magnifications. This irregularity indicates a non-uniform growth process in the absence of N doping. However, upon the introduction of N, as depicted in Figure 2d–f, the composite $N-V_2O_3/C$ transitions to a formation predominantly composed of nanospheres, exhibiting a more uniform and regular morphology.
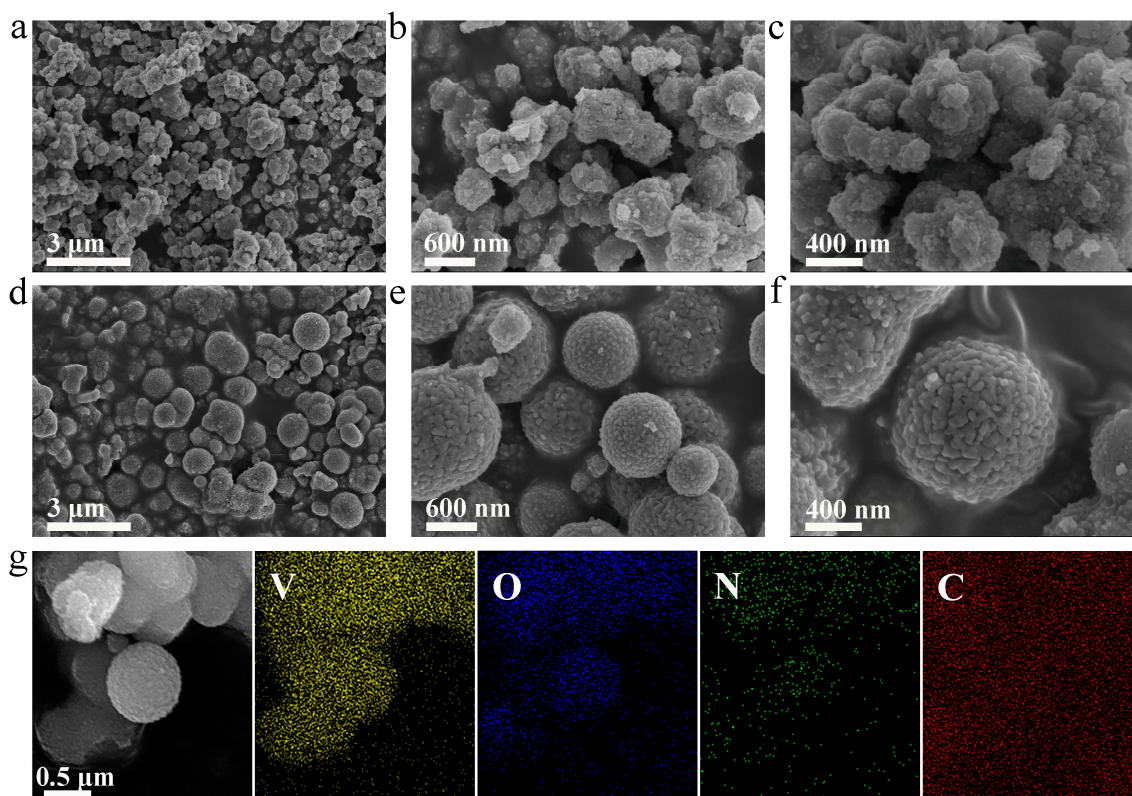


**Figure 2.** SEM at different multiples of (**a**–**c**) $V_2O_3/C$, (**d**–**f**) $N-V_2O_3/C$; (**g**) EDS mapping of $N-V_2O_3/C$.

The introduction of N atoms into the $V_2O_3/C$ composite's lattice structure fundamentally alters the surface energy and electronic configuration of the nanoparticles. N doping adjusts the surface properties by modifying the surface energy, which in turn influences the nucleation and growth processes of the nanoparticles. This modification facilitates a more isotropic growth mechanism, thereby promoting the development of a spherical morphology. The isotropic growth results from the uniform distribution of surface energy around the nanoparticle, leading to an equally distributed growth rate in all directions.

Furthermore, the doping of N enhances the uniformity in particle size, suggesting that N incorporation affects not just the surface energy but also the electronic properties of the nanoparticles. This change in electronic properties may influence the self-assembly process of the nanoparticles into nanospheres by altering the surface charge distribution and modifying interparticle interactions. Such alterations in the microscopic forces between particles could encourage a more orderly assembly process, favoring the formation of spheres over irregular shapes. This transformation suggests that N doping plays a critical role in controlling the nanostructure of the composite, thereby providing a tunable approach to modulate the material's microstructure for potential applications.

The energy-dispersive X-ray spectroscopy (EDS) mapping of $N-V_2O_3/C$, provided in Figure 2g, demonstrates a homogeneous distribution of the elements V, O, and N. The extensive presence of carbon is due to the conductive adhesive, highlighting its role in the composite's structure.

### 2.2. Electrochemically Induced Phase Transition

In this study, 3 M $Zn(CF_3SO_3)_2$ was employed as the electrolyte, with zinc foil serving as the anode and the synthesized products utilized as cathodes to fabricate button cells, aimed at evaluating their electrochemical performance. The initial tests involved constant current charge–discharge assessments, depicted in Figure 3a,d. Notably, a distinct difference was observed in the electrochemical profiles between the initial and subsequent cycles of the two cells, indicating a pronounced overcharging phenomenon.
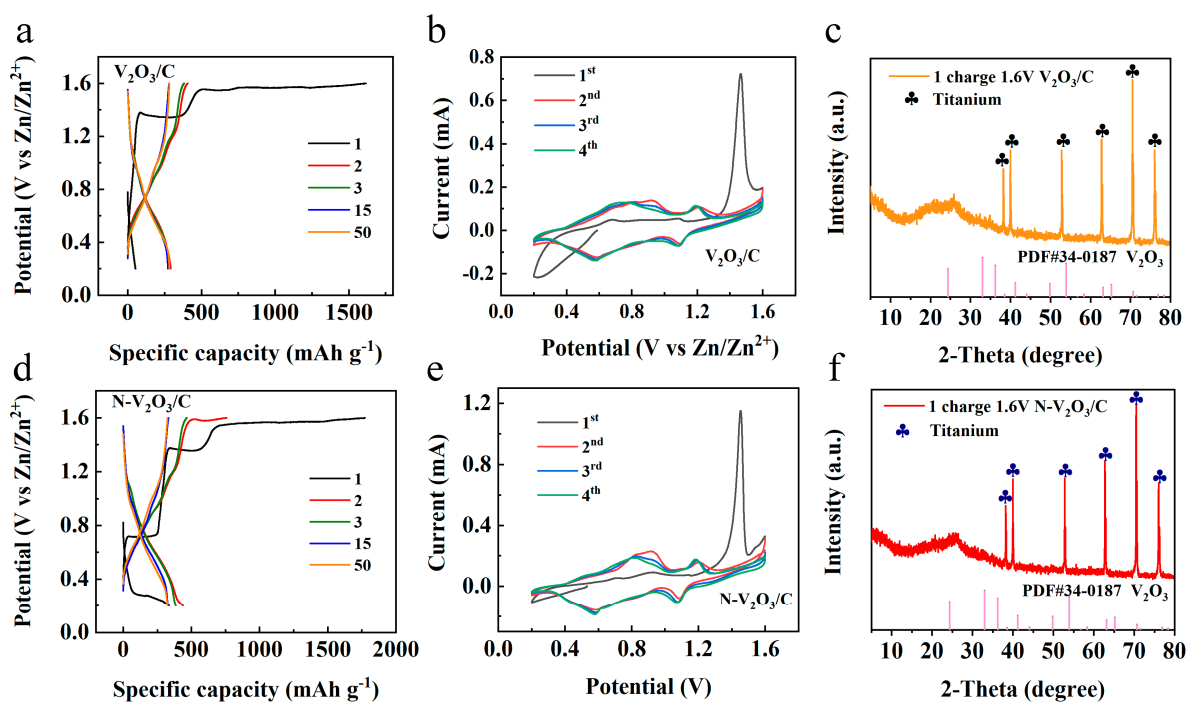


**Figure 3.** $V_2O_3/C$ of (**a**) constant current charge/discharge curve, (**b**) CV curve at 0.1 mV s$^{-1}$ sweep rate, (**c**) XRD pattern after the completion of the first charge; $N-V_2O_3/C$ of (**d**) constant current charge/discharge curve, (**e**) CV curve at 0.1 mV s$^{-1}$ sweep rate, (**f**) XRD patterns after the completion of the first charge.

For the cell incorporating $V_2O_3$/C as the cathode material, an initial discharge capacity of 52 mAh $g^{-1}$ was recorded, which significantly increased to a charging capacity of 1618 mAh $g^{-1}$. In the cycles that followed, the capacity reached a relatively stable value of approximately 284.3 mAh $g^{-1}$, with the observed voltage plateaus at 1.10/0.99 V and 0.62/0.87 V, respectively. Similarly, the cell featuring N-$V_2O_3$/C as the cathode exhibited an initial discharge capacity of 335.2 mAh $g^{-1}$ and a charging capacity of 1773.1 mAh $g^{-1}$. Subsequently, the capacity of this cell stabilized around 332.2 mAh $g^{-1}$, with voltage plateaus at 1.18/1.01 V and 0.68/0.87 V, respectively.

Cyclic voltammetry (CV) analysis was conducted at a scan rate of 0.1 mV $s^{-1}$ for both cells, with the results presented in Figure 3b,e. The analysis revealed a significant shift in the positions of oxidation and reduction peaks from the first cycle to subsequent cycles in both cells, indicative of irreversible phase transformations. Specifically, the initial cycle for $V_2O_3$/C was characterized by pronounced oxidation peaks at 0.68 and 1.52 V. In contrast, during the second cycle, these peaks were observed to migrate to 0.96/0.79 V and 1.22/1.09 V, respectively, with subsequent cycles demonstrating considerable overlap, implying the formation of a phase transition product with favorable reversibility. Similarly, the oxidation and reduction peak positions of N−$V_2O_3$/C closely matched those of $V_2O_3$/C, suggesting analogous reaction mechanisms. This alignment is corroborated by constant current charge and discharge profiles, which exhibited notable consistency across cycles, further confirming the reversibility of the phase transition product in a manner comparable to $V_2O_3$/C.

To gain comprehensive insights into the electrochemical changes occurring within the cells, XRD analyses were performed on the cathode materials post charging, as illustrated in Figure 3c,f. The analyses demonstrated that following the initial charging process, the distinct characteristic peaks of both $V_2O_3$/C and N−$V_2O_3$/C were eradicated, indicating a transformation to an amorphous, non-crystalline state.

The post-cycling morphological transformations of $V_2O_3$/C and N−$V_2O_3$/C electrodes were meticulously examined via scanning electron microscopy (SEM). The analysis revealed that throughout the course of the electrochemical reactions, the $V_2O_3$/C electrodes underwent a morphological evolution from irregularly shaped nanoparticles to nanorods of diminished diameter (refer to Figure 4a,b). In a contrasting manner, N−$V_2O_3$/C electrodes transitioned from well-defined nanospheres to nanosheets (illustrated in Figure 4c,d). This alteration significantly enhanced their specific surface area, thereby optimizing them for improved $Zn^{2+}$ ion storage capabilities.
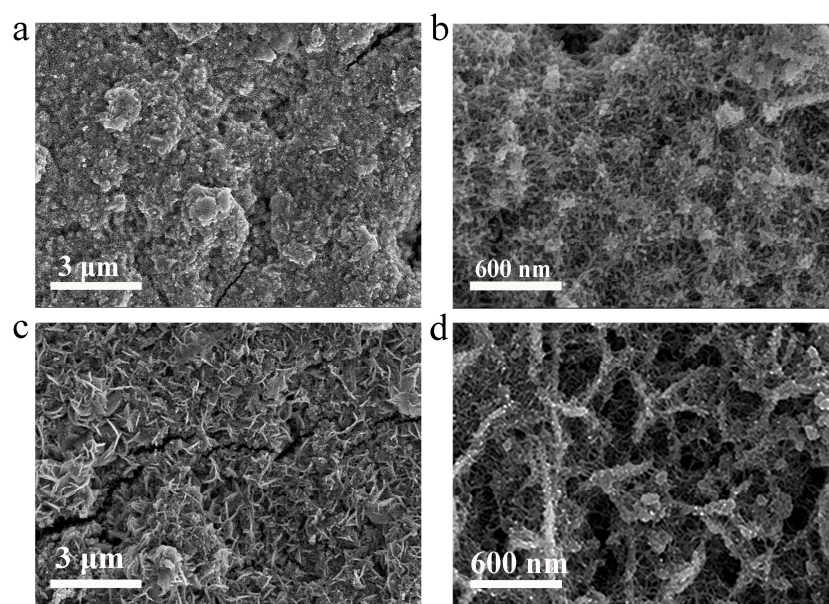


**Figure 4.** SEM images after cycle of (**a**,**b**) $V_2O_3$/C, (**c**,**d**) N−$V_2O_3$/C.

The morphological and microstructural evolutions of N-$V_2O_3$/C following its phase transition were meticulously characterized through high-resolution transmission electron microscopy (HRTEM). Prior to electrochemical cycling, Figure 5a delineates the material's initial structure as nanospheres encased by irregular entities, which were identified as amorphous carbon. The HRTEM imagery distinctly highlighted lattice fringes, elucidating that the introduction of nitrogen doping and carbon encapsulation preserved the crystalline integrity of $V_2O_3$.
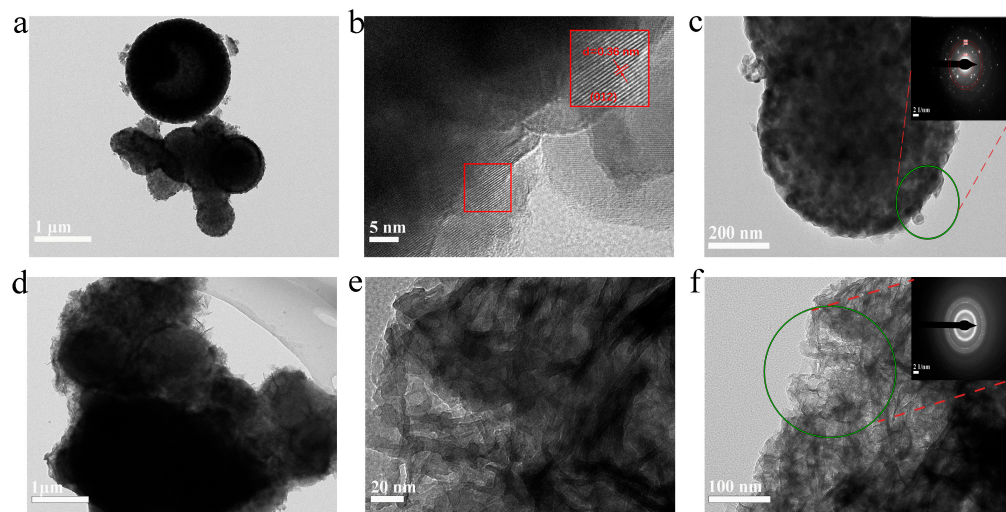


**Figure 5.** N−$V_2O_3$/C before cycling, (**a**) TEM image, (**b**) HRTEM image, (**c**) selected area electron diffraction; N−$V_2O_3$/C after cycling, TEM (**d,e**), (**f**) selected area electron diffraction.

This finding is in harmony with the crystallinity observations reported in the XRD analysis (refer to Figure 1c). The selected area electron diffraction (SAED) pattern of N-$V_2O_3$/C, depicted in Figure 5c, before cycling, exhibited luminous diffraction rings. These rings correspond to the (012), (024), and (018) crystallographic planes of $V_2O_3$, affirming the polycrystalline essence of the material. Post charging, the N−$V_2O_3$/C specimens transformed into more voluminous, albeit irregular and thinner structures, as illustrated in Figure 5d,e. The SAED pattern after cycling, shown in Figure 5f, revealed a diffuse halo devoid of sharp boundaries, a manifestation that aligns with the XRD findings post cycling. This unequivocally corroborates the electrochemical induction of a phase transition to an amorphous state after the initial cycle of charging and discharging.

In an effort to further elucidate the transition from crystalline to amorphous structures in vanadium oxides, density functional theory (DFT) calculations were conducted on the amorphous vanadium oxide (amorphous VO) system, with Zn introduced as a dopant. The results, illustrated in Figure 6a,b, showcase the density of states (DOS) and partial density of states (PDOS) for both the crystalline and amorphous VO structures, with a specific emphasis on the amorphous structure incorporating Zn.

The DFT findings indicate a significant peak at the Fermi level in the DOS of amorphous VO, primarily contributed by the 2p orbitals of oxygen. This feature highlights the metallic character of the system, which is associated with an enhanced electrical conductivity compared to its crystalline counterpart. The introduction of Zn into the amorphous VO structure further modifies the electronic environment. Specifically, Zn acts as an electron donor, transferring electrons predominantly to the oxygen's 2p orbitals. This electron transfer intensifies the metallic characteristics of the amorphous VO, as reflected by the enhanced peak at the Fermi level and the subsequent increase in electrical conductivity.

The augmentation of the oxygen 2p orbital contribution in the presence of Zn not only supports the enhanced conductivity but also suggests a pivotal role for oxygen in the electrochemical performance of the system. This alteration in the electronic structure is crucial for understanding the phase transition's impact on the material's electrochemical proper-

ties. The transition to an amorphous structure, induced by electrochemical cycling and substantiated by these DFT calculations, appears to enhance the system's electrochemical performance by fostering a more conducive electronic environment for charge transport.
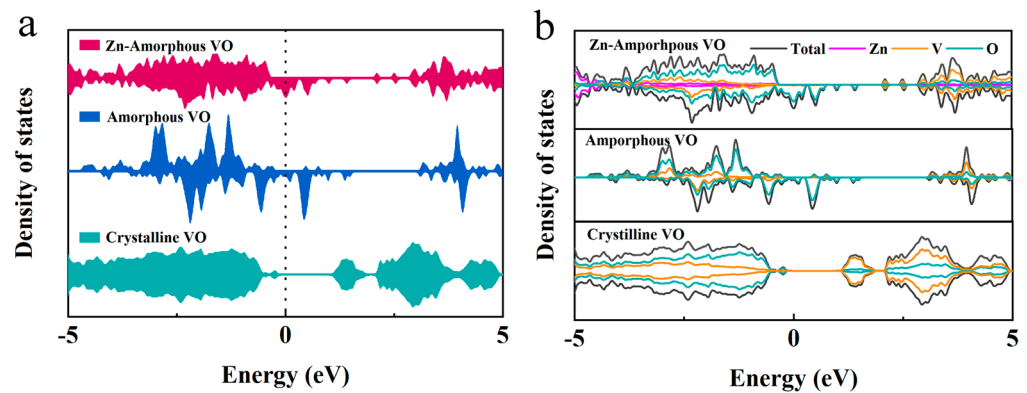


**Figure 6.** Crystalline VO, amorphous VO and Zn diffusion in amorphous VO (**a**) DOS, (**b**) PDOS.

XPS was utilized to elucidate the chemical compositions and the states of elements within $N-V_2O_3/C$, both prior to and subsequent to the inaugural charging cycle, with the findings illustrated in Figure 7. The survey spectrum, as presented in Figure 7a, confirmed the presence of N, vanadium (V), oxygen (O), and carbon (C) in the pristine $N-V_2O_3/C$. Notably, post charging, the spectrum also revealed the presence of Zn. A detailed examination of the V 2p fine spectrum, depicted in Figure 7b, revealed that the binding energies in the pristine sample were predominantly observed at 524.8/517.7 eV and 523.4/516.7 eV, indicative of the oxidation states $V^{4+}$ and $V^{5+}$, respectively. Following the charging process, the oxidation states of vanadium remained as $V^{4+}$ and $V^{5+}$. However, a discernible augmentation in the proportion of $V^{5+}$ was evident from the enhanced intensity and area of the respective peaks, setting a foundation for an escalated occurrence of redox reactions in the subsequent stages [31].
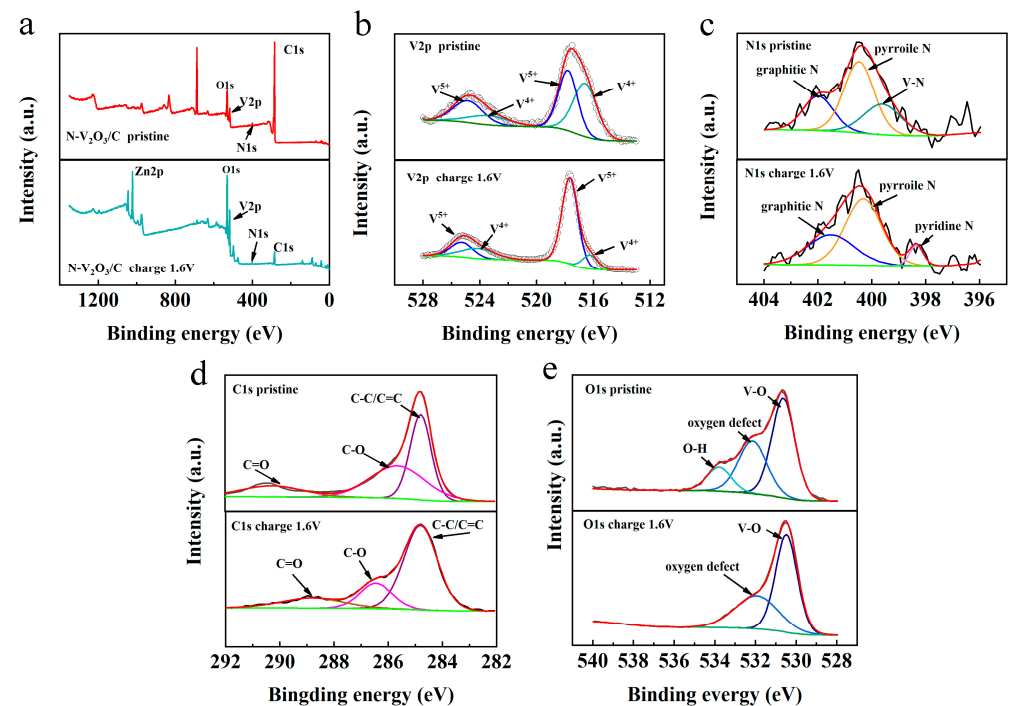


**Figure 7.** (**a**) XPS full spectrum information of $N-V_2O_3/C$; (**b**) XPS fine spectrum of V 2p in $N-V_2O_3/C$; (**c**) XPS high-resolution spectra of N 1s in $N-V_2O_3/C$; (**d**) XPS high-resolution spectra of C 1s in $N-V_2O_3/C$; (**e**) XPS high-resolution spectra of O 1s in $N-V_2O_3/C$.

The investigation into the N component within $N-V_2O_3/C$ unveiled that the initial N binding energies were predominantly positioned at 399.6, 400.4, and 401.8 eV. These correspond to $V-N$ bonds, pyrrolic N, and graphitic N, respectively, as illustrated in Figure 7c. Post charging, the formation of pyridinic N was observed, with both pyrrolic and pyridinic N exhibiting more negative electronegativities. This characteristic is advantageous for enhancing the transport rate of $Zn^{2+}$ ions.

As depicted in Figure 7d, the C 1s spectrum of the pristine $N-V_2O_3/C$ reveals binding energies at 284.9 eV, 285.8 eV, and 290.7 eV, which correspond to $C-C/C=C$, $C-O$, and $C=O$ bonds, respectively. These observations are indicative of a complex carbonaceous matrix within the composite, where both $sp^2$ and $sp^3$ hybridized carbon atoms coexist, facilitating a conducive environment for electron transport and structural stability. The presence of $C-O$ and $C=O$ functionalities suggests interactions between carbon and other components in the composite, which could play a pivotal role in the electrochemical performance of the material. Upon the completion of the charging cycle, a notable shift in the binding energies for $C-O$ and $C=O$ functionalities is observed, moving to 286.7 eV and 288.9 eV, respectively. This shift is attributed to the electrochemical interactions occurring during the charging process, leading to a reconfiguration of the electronic structure of carbon. These changes could enhance the electrochemical reactivity and facilitate the adsorption and desorption of ions, such as $Zn^{2+}$, on the surface of the $N-V_2O_3/C$, thereby improving the material's performance in energy storage applications.

In addition, as illustrated in Figure 7e, the O 1s spectrum from the initial $N-V_2O_3/C$ sample exhibits binding energies at 530.6 eV, 532.7 eV, and 534.2 eV, corresponding to $V-O$, oxygen vacancies, and $O-H$, respectively. The presence of $V-O$ signifies the strong interaction between vanadium and oxygen, crucial for the structural integrity and electrochemical activity of the oxide component. Oxygen vacancies, on the other hand, are known to enhance conductivity and promote redox reactions by serving as active sites. The $O-H$ component suggests the presence of hydroxyl groups or absorbed water, which could influence ion transport and surface chemistry. Following the charging process, the O 1s spectrum undergoes significant changes; the peak associated with $O-H$ disappears, while the peaks corresponding to $V-O$ and oxygen vacancies remain. This indicates the dehydration or removal of hydroxyl groups on the surface, potentially leading to increased conductivity and a more favorable environment for the transport and intercalation of $Zn^{2+}$ ions. The preservation of oxygen vacancies further supports the material's capacity for facilitating redox reactions, crucial for its electrochemical performance.

### 2.3. Electrochemical Performance

To investigate the post-phase transition electrochemical behavior of $V_2O_3/C$ and N-doped $V_2O_3/C$, these materials were utilized as cathodes within AZIBs. Initially subjected to a current density of 0.2 A g$^{-1}$, the cycling performance depicted in Figure 8a demonstrates that both $V_2O_3/C$ and $N-V_2O_3/C$ exhibited notably high specific capacities for both charging and discharging within the initial 10 cycles, alongside a coulombic efficiency surpassing 100%. This phenomenon is ascribed to the phase transition experienced by the cathode materials under subdued current densities, which precluded the attainment of a fully stable structural configuration, thereby leading to the misalignment of charge and discharge profiles. Beyond the preliminary 10 cycles, a commendable degree of stability was observed for both electrodes; $V_2O_3/C$ recorded a capacity of 284.6 mAh g$^{-1}$, whereas $N-V_2O_3/C$ demonstrated a superior capacity of 331.1 mAh g$^{-1}$. Subsequent to the initial evaluation, cycling performance at an escalated current density of 5 A g$^{-1}$ was assessed, as illustrated in Figure 8b. Mirroring the low-current density findings, an activation process for the electrodes was discernible. Following an extended cycling duration of approximately 150 cycles, a stabilization in the capacities was noted, with $V_2O_3/C$ attaining a capacity of 242.6 mAh g$^{-1}$ and $N-V_2O_3/C$ achieving a capacity of 264.1 mAh g$^{-1}$, each maintaining a coulombic efficiency of 100%.
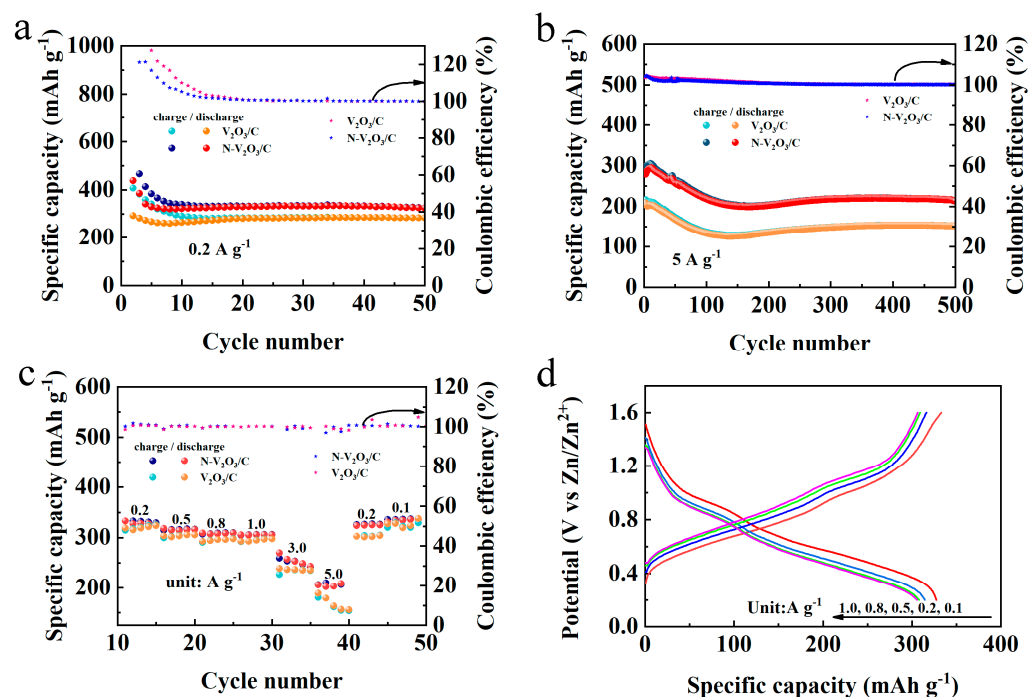
**Figure 8.** Electrochemical performance of $V_2O_3$/C and $N-V_2O_3$/C after phase change, (**a**) cycling performance at 0.2 A g$^{-1}$, (**b**) cycling performance at 5 A g$^{-1}$, (**c**) rate performance, (**d**) constant current charge–discharge curves at different current densities.

The rate performance of $V_2O_3$/C and $N-V_2O_3$/C following the stabilization of the phase transition was systematically evaluated across a spectrum of current densities, namely 0.2, 0.5, 0.8, 1.0, 3.0, and 5.0 A g$^{-1}$, as illustrated in Figure 8c. The initial observations reveal that, at lower current densities, the specific capacities of both materials exhibit considerable similarity. However, with an increment in current density, $N-V_2O_3$/C not only manifests enhanced specific capacities but also displays augmented stability, underscoring its remarkable resilience against high current demands. This finding aligns with the patterns discerned during the cycling performance assessments, where the augmented electrochemical robustness of $N-V_2O_3$/C was evident. Remarkably, upon the diminution of current densities, both $V_2O_3$/C and $N-V_2O_3$/C succeeded in reinstating their original specific capacities, thereby demonstrating their exceptional rate capabilities.

Further, Figure 8d delineates the constant current charge–discharge profiles for both electrodes across varying current densities, mirroring the observed rate performances. A noteworthy aspect of these profiles is the presence of two pronounced and analogous charge–discharge plateaus, pinpointed at 0.97/1.07 V and 1.02/1.22 V, respectively. These plateaus are in harmony with the oxidation and reduction peak positions previously identified in the CV analysis of $N-V_2O_3$/C.

Figure 9 delineates the enduring cycling performance of both $V_2O_3$/C and $N-V_2O_3$/C under a substantial current load of 10 A g$^{-1}$. In the initial cycles, $V_2O_3$/C demonstrated an initial specific capacity of 110.3 mAh g$^{-1}$ in contrast to $N-V_2O_3$/C, which registered a notably lower capacity of 40.6 mAh g$^{-1}$. However, an upward trajectory in the capacities of both materials was observed thereafter, a phenomenon attributed to the progressive activation of the electrodes. Upon reaching full activation, the specific capacities were recorded at 151.6 mAh g$^{-1}$ for $V_2O_3$/C and an elevated 168.4 mAh g$^{-1}$ for $N-V_2O_3$/C. Post 900 cycles, $V_2O_3$/C's capacity was reduced to 56.2 mAh g$^{-1}$, correlating to a capacity retention rate of 37%. Contrastingly, $N-V_2O_3$/C showcased remarkable endurance, maintaining a capacity of 160.5 mAh g$^{-1}$ even after 1000 cycles, which translates to an impressive retention rate of 95%. These findings underscore the substantial enhancement in capacity retention and cycling stability conferred by nitrogen doping.
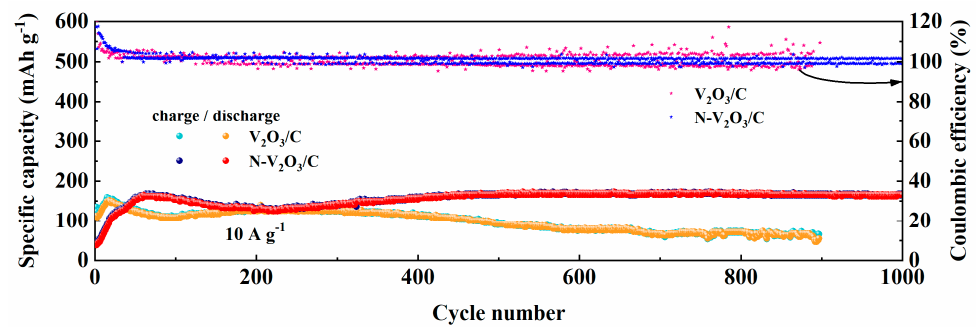
**Figure 9.** Long cycle performance of $V_2O_3/C$ and $N-V_2O_3/C$ at 10 A g$^{-1}$.

To elucidate the kinetic mechanisms underlying the electrochemical behavior of $V_2O_3/C$ and $N-V_2O_3/C$, CV analyses were conducted across a spectrum of scan rates (0.1, 0.2, 0.4, 0.6, 0.8, and 1.0 mV s$^{-1}$), with the results depicted in Figure 10a,d. The observations revealed analogous oxidation and reduction peaks for both materials, suggesting the occurrence of comparable electrochemical reactions. Notably, an escalation in scan rate led to a polarization-induced shift of these peaks to higher and lower potentials for oxidation and reduction processes, respectively. The empirical relationship between the peak current ($i$) and the scan rate ($v$) is formalized as follows:

$$i = av^b \tag{1}$$

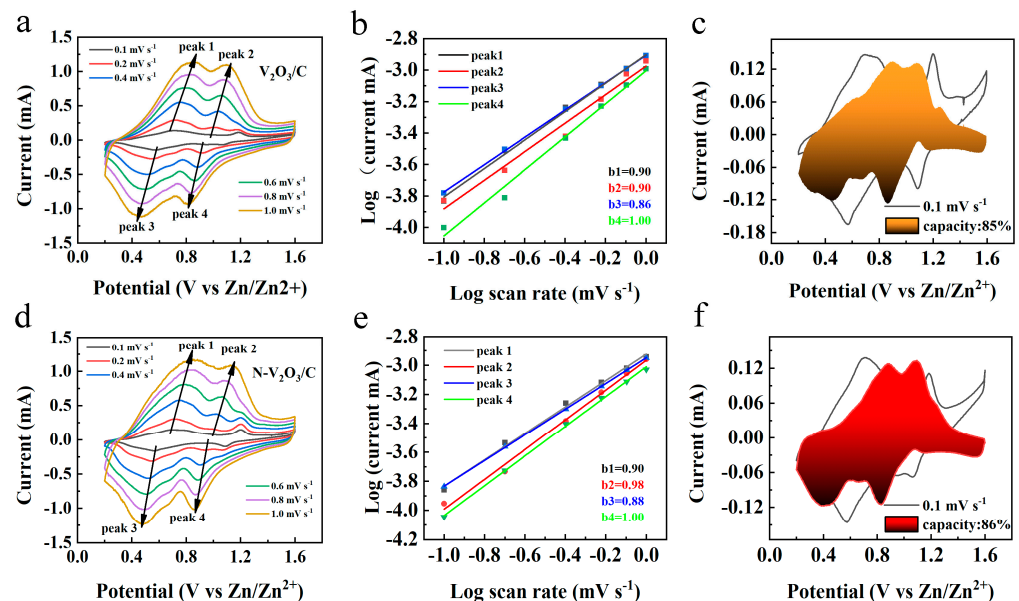$$\log(i) = \log(a) + b\log(v) \tag{2}$$



**Figure 10.** CV curves at different sweep speeds, (**a**) $V_2O_3/C$, (**d**) $N-V_2O_3/C$; linear fit curves of $\log(i)$ versus $\log(v)$ (**b**) $V_2O_3/C$, (**e**) $N-V_2O_3/C$; CV curves at 0.1 mV s$^{-1}$ sweep speed, (**c**) $V_2O_3/C$, (**f**) $N-V_2O_3/C$.

Within these formulations, parameters *a* and *b* are indicative of the system's electrochemical dynamics, with b serving as a determinant of the dominant control mechanism—diffusion or pseudocapacitance. Specifically, a *b* value nearing 1.0 is indicative of pseudocapacitive control, whereas a value approaching 0.5 signifies diffusion dominance. Intermediate *b* values suggest a mixed control mechanism. The linear regression analyses of $\log(i)$ versus $\log(v)$ for both $V_2O_3/C$ and $N-V_2O_3/C$, presented in Figure 10b,e, respectively, yielded *b* values predominantly within the range of 0.5 to 1.0, implying a significant influence from both diffusion and pseudocapacitance on the electrochemical

reactions. Crucially, a *b* value of 1.0 for both materials underscores the substantial role of pseudocapacitive behavior in certain electrode processes, contributing to their enhanced rate capabilities. Additionally, CV profiles at a scan rate of 0.1 mV s$^{-1}$ are showcased in Figure 10c,f, alongside the deduced pseudocapacitive contributions of 85% for $V_2O_3/C$ and 86% for $N-V_2O_3/C$.

Figure 11 illustrates the variation in pseudocapacitive contribution rates for the electrode materials $V_2O_3/C$ and $N-V_2O_3/C$ across a spectrum of scan rates. The pseudocapacitive contributions for $V_2O_3/C$ are recorded at 85%, 91%, 94%, 96%, 97%, and 98% for increasing scan rates, respectively. Conversely, the corresponding values for $N-V_2O_3/C$ are slightly higher, being 86%, 92%, 95%, 97%, 98%, and 99%, respectively. This upward trend in pseudocapacitance with escalating scan rates signifies a shift towards more capacitive-dominated electrochemical reactions for both materials, a trait that enhances cyclic durability especially under conditions of high current. Remarkably, the consistently higher pseudocapacitive contributions observed for $N-V_2O_3/C$ as compared to $V_2O_3/C$ underscore superior electrochemical kinetics. This distinction not only underpins an improved diffusion rate for $Zn^{2+}$ ions but also aligns with the observed enhancements in the cyclic and rate performances of the materials.
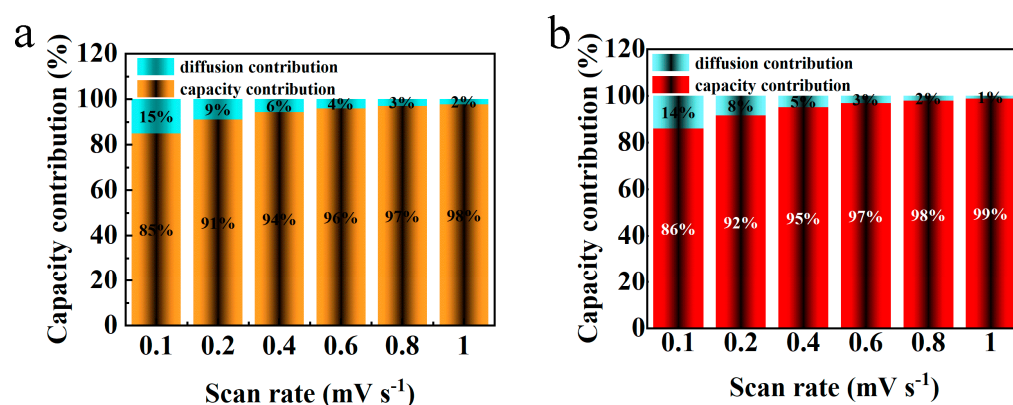


**Figure 11.** Capacitance contribution diagram at different sweep speeds, (**a**) $V_2O_3/C$, (**b**) $N-V_2O_3/C$.

Electrochemical impedance spectroscopy (EIS) analyses were executed employing an electrochemical workstation, with the outcomes illustrated in Figure 12a. These outcomes revealed a semicircle in the high-frequency range, indicative of charge transfer resistance, and a linear slope in the low-frequency range, indicative of ion diffusion processes. Importantly, the $N-V_2O_3/C$ exhibited a markedly reduced charge transfer resistance in comparison to $V_2O_3/C$, which aligned with their respective electrochemical performances. Upon conducting four cycles, a notable reduction was observed in both charge transfer resistance and ion diffusion for $N-V_2O_3/C$, as demonstrated in Figure 12b, thereby augmenting its electronic conductivity. This enhancement substantiates the observed initial capacity increment throughout the cycling process.

The $Zn^{2+}$ diffusion coefficient was quantified employing the galvanostatic intermittent titration technique (GITT), which substantiated the enhancement of ionic kinetics subsequent to nitrogen doping. The GITT experimentation was executed with a specified current density of 0.1 A g$^{-1}$, a relaxation time ($\tau$) of 30 min, and measurement intervals set at 60 s. Figure 13b reveals that the diffusion coefficient for $V_2O_3/C$ was observed to lie between $10^{-11}$ and $10^{-12}$ cm$^2$ s$^{-1}$. Conversely, for $N-V_2O_3/C$, the $Zn^{2+}$ diffusion coefficient was determined to be within the range of $10^{-10}$ to $10^{-11}$ cm$^2$ s$^{-1}$.
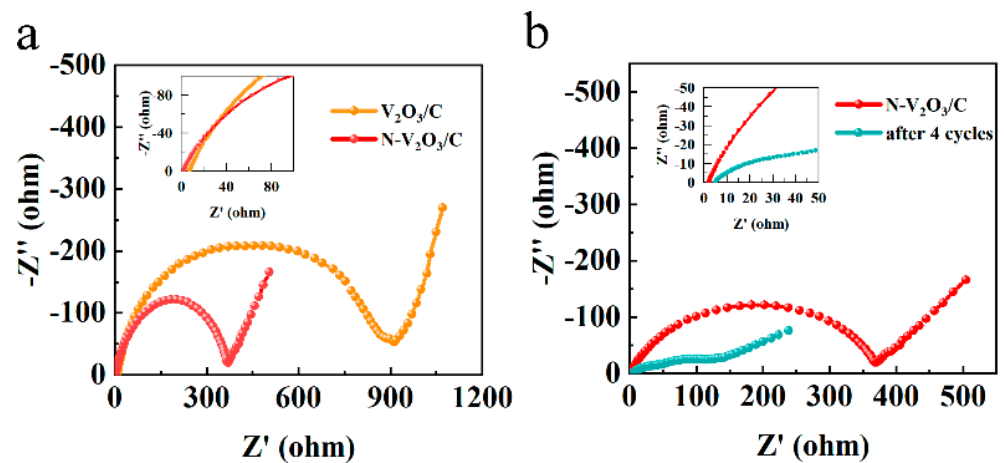
**Figure 12.** (**a**) Impedance of $V_2O_3/C$ and $N-V_2O_3/C$, (**b**) impedance of $N-V_2O_3/C$ after cycling.
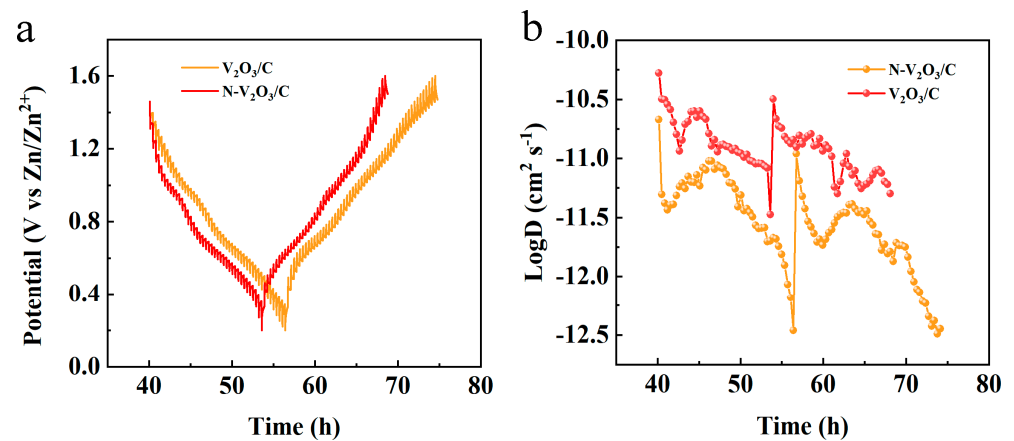


**Figure 13.** GITT curves of $V_2O_3/C$ and $N-V_2O_3/C$ (**a**) at current density of 0.1 A g$^{-1}$, (**b**) Zn$^{2+}$ diffusion coefficient.

### 2.4. Mechanistic Investigation

To elucidate the zinc storage mechanism within the $N-V_2O_3/C$ matrix following its electrochemically induced phase transition, ex situ XRD analyses were conducted throughout the third charge/discharge cycle. As shown in Figure 14b, minimal alterations in the peak positions were observed during the initial discharge phase, consistent with the patterns noted after the first charge cycle (refer to Figure 3f). Notably, upon discharging to 0.8 V, a new peak emerged at 22.4°, indicative of a chemical reaction between Zn$^{2+}$ ions and $N-V_2O_3/C$, leading to the formation of the $Zn-(N-V_2O_3/C)$ complex. The intensity of this peak increased significantly upon further discharging to 0.2 V. In contrast, as the cell was charged to 0.9 V and eventually reached 1.6 V, the intensity of this peak decreased, and upon completion of the charging process, all peaks indicative of intermediate phases were no longer detectable. This behavior highlights the pronounced reversibility of the structure with respect to the intercalation and deintercalation processes of Zn$^{2+}$ ions.

XPS analyses were performed to investigate the elemental state transformations in $N-V_2O_3/C$ during the third charge/discharge cycle. Initially, the Zn 2p spectrum displayed no detectable Zn signals (Figure 15a). This changed upon discharging the material to 0.2 V, where a prominent pair of Zn 2p peaks at 1022.2 eV and 1045.1 eV emerged, indicative of the successful intercalation of Zn$^{2+}$ ions. Upon recharging to 1.6 V, the intensity of these Zn 2p peaks significantly decreased, though they did not disappear entirely, suggesting a partial and potentially irreversible incorporation of Zn$^{2+}$ ions.
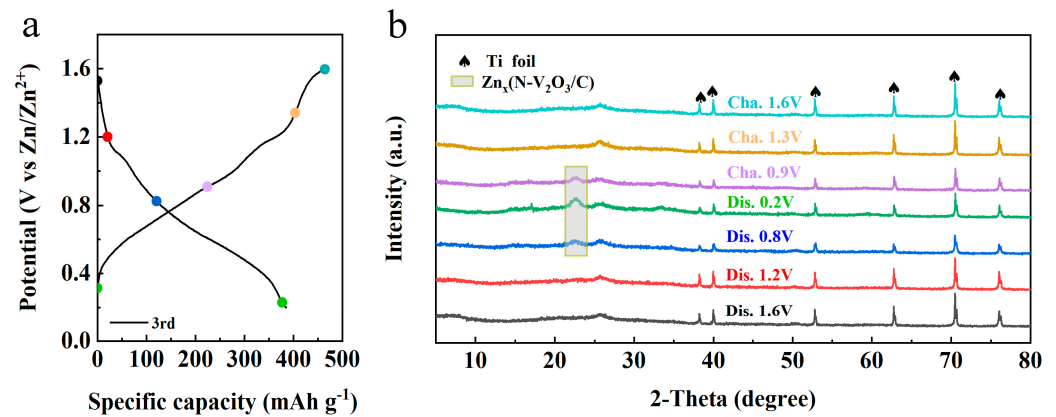
**Figure 14.** (**a**) Third constant current charge–discharge curve of $N-V_2O_3/C$ at a current density of 0.1 A g$^{-1}$, (**b**) ex-XRD of $N-V_2O_3/C$ during the third charge–discharge.
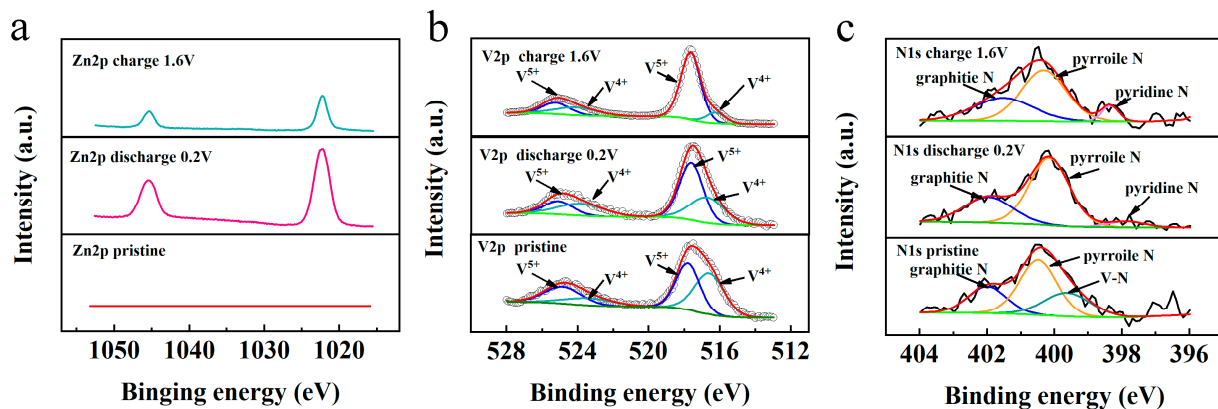


**Figure 15.** Ex-XPS during the third charge–discharge of $N-V_2O_3/C$, (**a**) Zn 2p, (**b**) V 2p, and (**c**) N 1s.

The valence state dynamics of vanadium are detailed in Figure 15b. Initial spectra exhibited two peak pairs located at 524.8/517.7 eV and 523.4/516.7 eV, corresponding to the $V^{4+}$ and $V^{5+}$ oxidation states in V 2p3/2, respectively. Discharging the cell to 0.2 V resulted in a noticeable shift in the $V^{4+}/V^{5+}$ ratio, which was further modified upon recharging to 1.6 V. At this stage, an increase in the $V^{5+}$ content was observed, indicating a reversion of vanadium valence states post $Zn^{2+}$ deintercalation.

Additionally, changes in the chemical state of nitrogen were monitored through the N 1s spectra (Figure 15c). A marginal increase in pyridinic nitrogen content was detected following discharge to 0.2 V, which intensified upon complete recharge. This alteration is proposed to facilitate the accelerated diffusion rate of $Zn^{2+}$ ions in $N-V_2O_3/C$ compared to its $V_2O_3/C$ counterpart during the electrochemical cycle. This comprehensive analysis underscores the complex interplay of ionic and electronic changes within $N-V_2O_3/C$ that significantly impact its electrochemical behavior.

### 2.5. Investigation of Nitrogen Content

To investigate the impact of nitrogen doping levels on performance, the synthesis process involved varying the molar ratios of the vanadium source acetylacetonate vanadium to the nitrogen source thiourea as 2:1, 2:2, 2:3, and 2:4, using 0.076 g, 0.152 g, 0.228 g, and 0.304 g of thiourea, respectively. These were designated as $N-V_2O_3/C-1$, $N-V_2O_3/C-2$, $N-V_2O_3/C-3$, and $N-V_2O_3/C-4$, respectively.

From the cycling performance at a current density of 0.2 A g$^{-1}$ (Figure 16a), it can be observed that these materials all undergo similar cycling experiences. In the first 10 charge–discharge cycles, their charge and discharge profiles do not overlap, with the coulombic efficiency exceeding 100%, indicative of a transition from phase change to stability. After

10 cycles, the charge and discharge begin to stabilize, among which $N-V_2O_3/C-3$ exhibits the highest capacity after 50 cycles, reaching 331.1 mAh g$^{-1}$. Figure 16b presents the cycling performance at a current density of 5 A g$^{-1}$. It is evident that their cycling processes are similar, among which $N-V_2O_3/C-3$ has the highest initial capacity. When reaching a stable cycle, $N-V_2O_3/C-2$ exhibits a relatively higher capacity, but its retention rate is not as favorable. After 500 cycles, $N-V_2O_3/C-3$ shows the highest capacity and the best retention rate, achieving 111%.
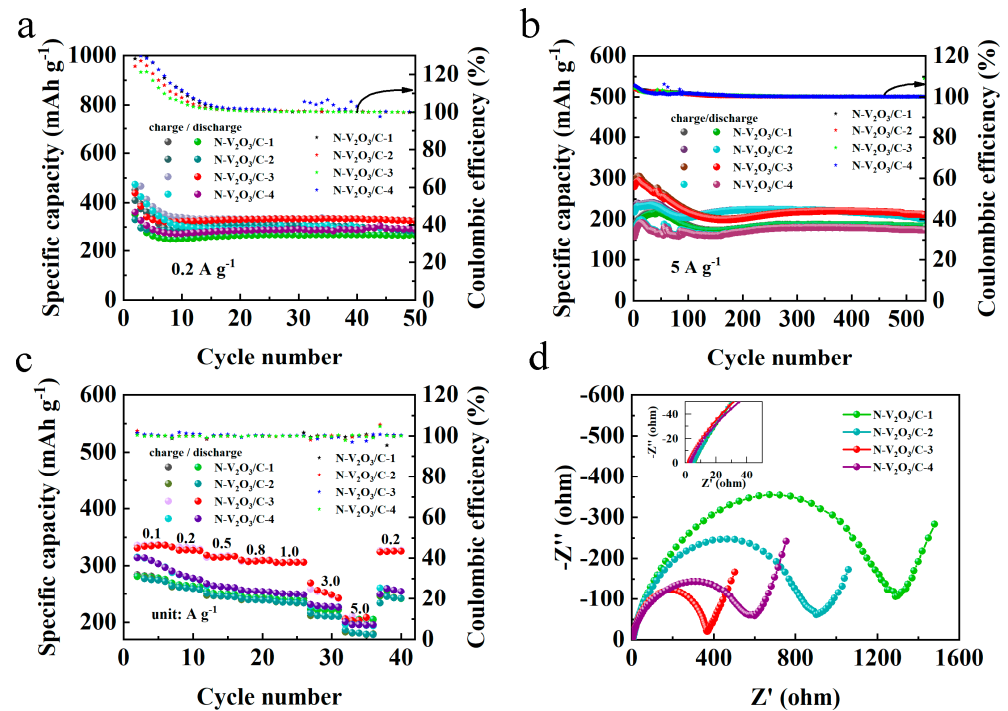


**Figure 16.** Electrochemical performance of $N-V_2O_3/C-1$, $N-V_2O_3/C-2$, $N-V_2O_3/C-3$, and $N-V_2O_3/C-4$, (**a**) cycling performance at 0.2 A g$^{-1}$, (**b**) cycling performance at 5 A g$^{-1}$, (**c**) rate performance at different current densities, (**d**) impedance.

In Figure 16c, the rate performance of $N-V_2O_3/C$ electrodes, with varying levels of nitrogen doping, is evaluated across a series of current densities: 0.1, 0.2, 0.5, 0.8, 1.0, 3.0, and 5.0 A g$^{-1}$. Notably, the electrode designated $N-V_2O_3/C-3$ consistently demonstrated the most superior capacity, exhibiting negligible variation over the tested current density range. Furthermore, this electrode's ability to recover its initial capacity upon the reduction in current density to lower rates signifies its exceptional rate capability. Electrochemical impedance spectroscopy (EIS) analysis, depicted in Figure 16d, reveals that $N-V_2O_3/C-3$ possesses the minimal electrochemical charge transfer and ionic diffusion resistances among the tested materials, establishing a robust basis for its outstanding electrochemical attributes. The observed lower contact resistance of $N-V_2O_3/C-3$ also provides insight into its enhanced initial capacity, further validating the material's electrochemical efficiency.

The long-term cycling stability of $N-V_2O_3/C$ electrodes, differentiated by their nitrogen content, was rigorously evaluated under a high current density condition of 10 A g$^{-1}$. As depicted in Figure 17, a trend towards stabilization was observed for all materials after the initial 100 cycles. Upon extending the cycling to 1000 cycles, the following observations were made: $N-V_2O_3/C-1$ demonstrated a stable capacity of 135.7 mAh g$^{-1}$, maintaining a retention rate of 100%. $N-V_2O_3/C-2$ recorded a capacity of 87.1 mAh g$^{-1}$, with a significantly lower retention rate of 51%. $N-V_2O_3/C-3$ showcased a superior capacity of 168.5 mAh g$^{-1}$, accompanied by a retention rate of 102%, whereas $N-V_2O_3/C-4$ achieved a capacity of 109.9 mAh g$^{-1}$, marking the highest retention rate among the samples at 111%. Notably, while $N-V_2O_3/C-4$ exhibited the highest retention rate, its initial capacity

was comparatively lower. Conversely, N−V$_2$O$_3$/C-3 not only presented the highest initial capacity but also maintained a relatively high retention rate, underscoring that the electrochemical performance reached its zenith when the vanadium and nitrogen sources were combined at a molar ratio of 2:3. This composition was found to yield the most favorable outcomes in terms of both capacity and durability.
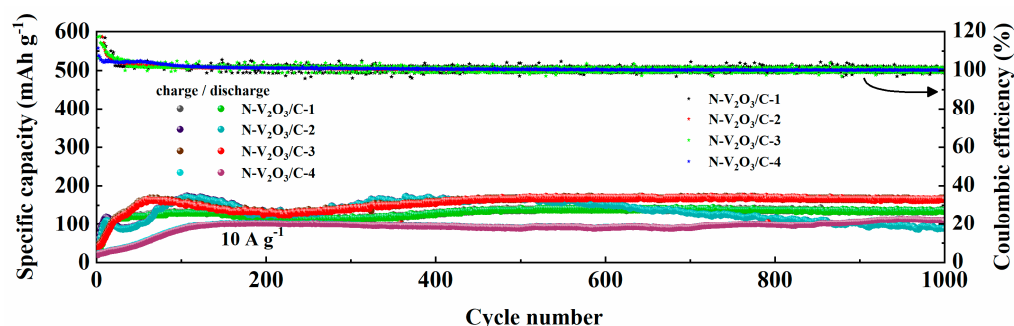


**Figure 17.** Long cycle performance of N−V$_2$O$_3$/C−1, N−V$_2$O$_3$/C−2, N−V$_2$O$_3$/C−3, and N−V$_2$O$_3$/C−4 at 10 A g$^{-1}$.

## 3. Materials and Methods

### 3.1. Preparation of Material

Initially, following a molar ratio of vanadium source to nitrogen source of 2:1, 0.6 g of acetylacetonate vanadium, 0.152 g of thiourea, and 0.4 g of glucose were dissolved in 70 mL of isopropanol and sonicated for 60 min. Subsequently, the solution was transferred into a 100 mL autoclave and maintained at 180 °C for 24 h. After the autoclave cooled down, the product was washed several times with ethanol and dried at 80 °C for 12 h to obtain the precursor. The obtained precursor was then calcined in a tube furnace under an argon atmosphere at 600 °C for 2 h with a heating rate of 10 °C per minute. This process yielded nitrogen-doped carbon-coated V$_2$O$_3$, designated as N−V$_2$O$_3$/C. By excluding thiourea from the reactants under otherwise identical conditions, carbon-coated V$_2$O$_3$, named V$_2$O$_3$/C, was obtained.

To investigate the impact of nitrogen doping levels on performance, the synthesis was carried out by varying the molar ratios of the vanadium source, acetylacetonate vanadium, to the nitrogen source, thiourea, as 2:1, 2:2, 2:3, and 2:4, using 0.076 g, 0.152 g, 0.228 g, and 0.304 g of thiourea, respectively. These were designated as N−V$_2$O$_3$/C−1, N−V$_2$O$_3$/C−2, N−V$_2$O$_3$/C−3, and N−V$_2$O$_3$/C−4, respectively.

### 3.2. Structure and Morphology Characterization

The physical and structural properties of all materials prepared during the electrochemical process were identified and analyzed using Cu Kα radiation (XRD, Smart Lab SE, Tokyo, Japan). The morphology and crystalline structure of the materials were characterized using an SEM (Hitachi SU8010, Tokyo, Japan) and a TEM (FEI Talos F200X, Waltham, MA, USA). The elemental distribution was characterized using the SEM-EDX method. The elemental composition of and valence state changes in powder samples and electrode slices were analyzed using XPS (Thermo ESCALAB 250Xi, Waltham, MA, USA).

### 3.3. Electrode Fabrication

The preparation process involved the mixing of the active material, acetylene black (as the conductive agent), and poly(1,1-difluoroethylene) (serving as the binder) in a mass ratio of 6:3:1. Following extensive milling, N-methyl-2-pyrrolidone (NMP) was incrementally added to achieve a homogenous slurry. This slurry was subsequently applied to a titanium foil substrate, which possessed a thickness of 0.1 mm. The coated substrate underwent a vacuum drying process at a temperature of 110 °C for a duration of 12 h. Post drying, the resultant film was sectioned into discs with a diameter of 10 mm, each containing an active material load ranging from 0.8 to 1.2 mg.

For the electrochemical cell assembly, zinc metal sheets were employed as the anodic material, whereas filter paper (specified by GB/T1914-2007 standards [32]) functioned as the separator. The titanium foil was utilized as the current collector and a 3 M solution of $Zn(CF_3SO_3)_2$ in the electrolyte. The assembly of the cell was performed under ambient conditions, followed by its hydraulic sealing utilizing a specialized battery sealing apparatus. Subsequent to the assembly, the cell was allowed to equilibrate for a period of 12 h prior to the initiation of electrochemical testing.

### 3.4. Electrochemical Measurements

In the experimental setup for the evaluation of electrochemical cells, a CR2032-type coin cell configuration was utilized as the prototype structure. The assembly of these cells incorporated zinc foil as the anode material and titanium foil as the current collector, with filter paper acting as the electrolyte separator. The entire cell assembly process was conducted in an electrolytic solution of 3 M $Zn(CF_3SO_3)_2$, under standard laboratory conditions at ambient temperature. For the electrochemical characterization of these cells, CV and EIS analyses were performed using a CHI 760E electrochemical workstation within a predefined voltage range of 0.2 to 1.8 V. Additionally, the LAND battery testing system was employed to meticulously evaluate the electrochemical performance of the assembled cells under study.

### 3.5. Calculation Method

DFT calculations were performed using the Vienna Ab initio Simulation Package (VASP) [33]. Exchange–correlation interactions were modeled using the Perdew–Burke–Ernzerhof (PBE) functional [34]. The computational setup utilized a plane-wave basis set with a cutoff energy of 400 eV, in conjunction with the projector augmented wave (PAW) method [35,36]. Convergence criteria for the self-consistent field iterations and the force calculations were established at $1 \times 10^{-5}$ eV and 0.01 eV Å$^{-1}$, respectively. The Brillouin zone sampling for the relaxation of the geometric structure and total energy calculations was conducted with a $2 \times 4 \times 1$ Γ-centered k-point mesh. To achieve higher resolution in the density of states calculations, an $8 \times 8 \times 1$ Γ-centered k-mesh was implemented.

## 4. Conclusions

In summary, we synthesized $N-V_2O_3/C$ using a hydrothermal method and evaluated its electrochemical performance as a cathode material for AZIBs in comparison with $V_2O_3/C$. The initial charge–discharge cycles revealed that both electrode types experienced phase transitions, resulting in the formation of amorphous vanadium oxides. This transformation significantly enhanced the electrical conductivity within the battery system. Notably, the integration of pyridinic and pyrrolic nitrogen into the structure of the nitrogen-doped electrode materials was found to substantially improve electronic conductivity, capacity, and electrochemical kinetics. Specifically, $N-V_2O_3/C$ demonstrated a remarkable capacity of 168.4 mAh g$^{-1}$ at a high current density of 10 A g$^{-1}$. A detailed analysis of the zinc storage mechanism in the phase-transformed products identified the emergence of intermediate species during the charge–discharge cycle, which subsequently vanished upon full charge, indicating a high degree of reversibility. Moreover, a systematic investigation into the effect of the nitrogen doping concentration revealed that the electrochemical performance of $N-V_2O_3/C$ was notably superior when prepared with a vanadium-to-nitrogen molar ratio of 2:3, thereby achieving the most favorable outcomes.

**Author Contributions:** Conceptualization, H.L. and H.C.; methodology, H.L. and Y.Z.; software, Y.Z.; validation, H.L., H.C. and Y.Z.; formal analysis, H.L. and H.C.; investigation, H.L., H.C. and Y.Z.; resources, H.C.; data curation, Y.Z.; writing—original draft preparation, H.L.; writing—review and editing, H.L., H.C. and Y.Z.; visualization, H.C. and Y.Z.; supervision, H.L.; project administration, H.L.; funding acquisition, H.L. All authors have read and agreed to the published version of the manuscript.

**Data Availability Statement:** The data presented in this study are available on request from the corresponding author.

**Conflicts of Interest:** The authors declare no conflicts of interest.

## References

1. Algarni, S.; Tirth, V.; Alqahtani, T.; Alshehery, S.; Kshirsagar, P. Contribution of renewable energy sources to the environmental impacts and economic benefits for sustainable development. *Sustain. Energy Technol. Assess.* **2023**, *56*, 103098. [CrossRef]
2. Franssen, T.; de Wilde, M. A clean energy future isn't set in stone. *Nat. Geosci.* **2021**, *14*, 636–637. [CrossRef]
3. Zheng, Y.; Yao, Y.; Ou, J.; Li, M.; Luo, D.; Dou, H.; Li, Z.; Amine, K.; Yu, A.; Chen, Z. A review of composite solid-state electrolytes for lithium batteries: Fundamentals, key materials and advanced structures. *Chem. Soc. Rev.* **2020**, *49*, 8790–8839. [CrossRef]
4. Xu, J.; Cai, X.; Cai, S.; Shao, Y.; Hu, C.; Lu, S.; Ding, S. High-energy lithium-ion batteries: Recent progress and a promising future in applications. *Energy Environ. Mater.* **2023**, *6*, e12450. [CrossRef]
5. Wang, Y.; Chen, R.; Chen, T.; Lv, H.; Zhu, G.; Ma, L.; Wang, C.; Jin, Z.; Liu, J. Emerging non-lithium ion batteries. *Energy Storage Mater.* **2023**, *4*, 103–129. [CrossRef]
6. Song, M.; Tan, H.; Chao, D.; Fan, H.J. Recent advances in Zn-ion batteries. *Adv. Funct. Mater.* **2018**, *28*, 1802564. [CrossRef]
7. Nie, C.; Wang, G.; Wang, D.; Wang, M.; Gao, X.; Bai, Z.; Wang, N.; Yang, J.; Xing, Z.; Dou, S. Recent progress on Zn anodes for advanced aqueous zinc-ion batteries. *Adv. Energy Mater.* **2023**, *13*, 2300606. [CrossRef]
8. Yan, H.; Zhang, X.; Yang, Z.; Xia, M.; Xu, C.; Liu, Y.; Yu, H.; Zhang, L.; Shu, J. Insight into the electrolyte strategies for aqueous zinc ion batteries. *Coordin. Chem. Rev.* **2022**, *452*, 214297. [CrossRef]
9. Shuai, H.; Liu, R.; Li, W.; Yang, X.; Lu, H.; Gao, Y.; Xu, J.; Huang, K. Recent advances of transition metal sulfides/selenides cathodes for aqueous zinc-ion batteries. *Adv. Energy Mater.* **2023**, *13*, 2202992. [CrossRef]
10. Li, H.; Ma, L.; Han, C.; Wang, Z.; Liu, Z.; Tang, Z.; Zhi, C. Advanced rechargeable zinc-based batteries: Recent progress and future perspectives. *Nano Energy* **2023**, *62*, 550–587. [CrossRef]
11. Wang, X.; Zhang, Z.; Xi, B.; Chen, W.; Jia, Y.; Feng, J.; Xiong, S. Advances and perspectives of cathode storage chemistry in aqueous zinc-ion batteries. *ACS Nano* **2021**, *15*, 9244–9272. [CrossRef] [PubMed]
12. Gao, S.; Zhang, Z.; Mao, F.; Liu, P.; Zhou, Z. Advances and strategies of electrolyte regulation in Zn-ion batteries. *Mater. Chem. Front.* **2023**, *7*, 3232–3258. [CrossRef]
13. Chen, L.; An, Q.; Mai, L. Recent advances and prospects of cathode materials for rechargeable aqueous zinc-ion batteries. *Adv. Mater. Interfaces* **2019**, *6*, 1900387. [CrossRef]
14. Li, G.; Sun, L.; Zhang, S.; Zhang, C.; Jin, H.; Davey, K.; Liang, G.; Liu, S.; Mao, J.; Guo, Z. Developing cathode materials for aqueous zinc ion batteries: Challenges and practical prospects. *Adv. Energy Mater.* **2024**, *34*, 2301291. [CrossRef]
15. Wang, S.; Zhang, H.; Zhao, K.; Liu, W.; Luo, N.; Zhao, J.; Wu, S.; Ding, J.; Fang, S.; Cheng, F. Designing interstitial boron-doped tunnel-type vanadium dioxide cathode for enhancing zinc ion storage capability. *Carbon Energy* **2023**, *5*, e330. [CrossRef]
16. Xu, X.; Xiong, F.; Meng, J.; Wang, X.; Niu, C.; An, Q.; Mai, L. Vanadium-based nanomaterials: A promising family for emerging metal-ion batteries. *Adv. Funct. Mater.* **2020**, *30*, 1904398. [CrossRef]
17. Yan, M.; He, P.; Chen, Y.; Wang, S.; Wei, Q.; Zhao, K.; Xu, X.; An, Q.; Shuang, Y.; Shao, Y.; et al. Water-lubricated intercalation in $V_2O_5 \cdot nH_2O$ for high-capacity and high-rate aqueous rechargeable zinc batteries. *Adv. Mater.* **2018**, *30*, 1703725. [CrossRef] [PubMed]
18. Wang, X.; Li, Y.; Wang, S.; Zhou, F.; Das, P.; Sun, C.; Zheng, S.; Wu, Z.-S. 2D amorphous $V_2O_5$/graphene heterostructures for high-safety aqueous Zn-ion batteries with unprecedented capacity and ultrahigh rate capability. *Adv. Energy Mater.* **2020**, *10*, 2000081. [CrossRef]
19. Zhang, Y.; Qin, J.; Batmunkh, M.; Li, W.; Fu, H.; Wang, L.; Al-Mamun, M.; Qi, D.; Liu, P.; Zhang, S.; et al. Scalable spray drying production of amorphous $V_2O_5$–EGO 2D heterostructured xerogels for high-rate and high-capacity aqueous zinc ion batteries. *Small* **2022**, *18*, 2105761. [CrossRef]
20. Li, Z.; Ren, Y.; Mo, L.; Liu, C.; Hsu, K.; Ding, Y.; Zhang, X.; Li, X.; Hu, L.; Ji, D.; et al. Impacts of oxygen vacancies on zinc ion intercalation in $VO_2$. *ACS Nano* **2020**, *14*, 5581–5589. [CrossRef]
21. Zhang, Z.; Xi, B.; Wang, X.; Ma, X.; Chen, W.; Feng, J.; Xiong, S. Oxygen defects engineering of $VO_2 \cdot xH_2O$ nanosheets via in situ polypyrrole polymerization for efficient aqueous zinc ion storage. *Adv. Funct. Mater.* **2021**, *31*, 2103070. [CrossRef]
22. Zhu, Q.; Xiao, Q.; Zhang, B.; Yan, Z.; Liu, X.; Chen, S.; Ren, Z.; Yu, Y. $VS_4$ with a chain crystal structure used as an intercalation cathode for aqueous Zn-ion batteries. *J. Mater. Chem. A* **2020**, *8*, 10761–10766. [CrossRef]

23. Shi, H.-Y.; Song, Y.; Qin, Z.; Li, C.; Guo, D.; Liu, X.-X.; Sun, X. Inhibiting $VOPO_4 \cdot x\,H_2O$ decomposition and dissolution in rechargeable aqueous zinc batteries to promote voltage and capacity stabilities. *Angew. Chem. Int. Edit.* **2019**, *58*, 16057–16061. [CrossRef] [PubMed]

24. Wei, S.; Chen, S.; Su, X.; Qi, Z.; Wang, C.; Ganguli, B.; Zhang, P.; Zhu, K.; Cao, Y.; He, Q.; et al. Manganese buffer induced high-performance disordered MnVO cathodes in zinc batteries. *Energy Environ. Sci.* **2021**, *14*, 3954–3964. [CrossRef]

25. Shan, L.; Zhou, J.; Zhang, W.; Xia, C.; Guo, S.; Ma, X.; Fang, G.; Wu, X.; Liang, S. Highly reversible phase transition endows $V_6O_{13}$ with enhanced performance as aqueous zinc-ion battery cathode. *Energy Technol.* **2019**, *7*, 1900022. [CrossRef]

26. Hao, Z.; Jiang, W.; Zhu, K. Carbon-encapsulated $V_2O_3$ nanorods for high-performance aqueous Zn-ion batteries. *Front. Chem.* **2022**, *10*, 956610. [CrossRef] [PubMed]

27. Zhu, K.; Wei, S.; Shou, H.; Shen, F.; Chen, S.; Zhang, P.; Wang, C.; Cao, Y.; Guo, X.; Luo, M.; et al. Defect engineering on $V_2O_3$ cathode for long-cycling aqueous zinc metal batteries. *Nat. Commun.* **2021**, *12*, 6878. [CrossRef]

28. Chen, H.; Rong, Y.; Yang, Z.; Deng, L.; Wu, J. $V_2O_3$@amorphous carbon as a cathode of zinc ion batteries with high stability and long cycling life. *Ind. Eng. Chem. Res.* **2021**, *60*, 1517–1525. [CrossRef]

29. Xing, Z.; Xu, G.; Han, J.; Chen, G.; Lu, B.; Liang, S.; Zhou, J. Facing the capacity fading of vanadium-based zinc-ion batteries. *Trends Chem.* **2023**, *5*, 380–392. [CrossRef]

30. Ou, L.; Liu, Z.; Zhou, Y.; Ou, H.; Zhu, J.; Cao, X.; Fang, G.; Zhou, J.; Liang, S. Pseudocapacitance-dominated zinc storage enabled by nitrogen-doped carbon stabilized amorphous vanadyl phosphate. *Chem. Eng. J.* **2021**, *426*, 131868. [CrossRef]

31. Yuan, J.; Gan, Y.; Mou, J.; Ma, X.; Li, X.; Meng, J.; Xu, L.; Zhang, X.; He, H.; Liu, J. Electrochemically induced amorphous and porous $VO_x$/N-doped carbon spheres as a cathode for advanced aqueous zinc-ion batteries. *Inorg. Chem. Front.* **2023**, *10*, 984–990. [CrossRef]

32. *GB/T1914-2007*; Chemical Analytical Filter Paper. Standards Press of China: Beijing, China, 2007.

33. Kresse, G.; Furthmüller, J. Efficient iterative schemes for ab initio total-energy calculations using a plane-wave basis set. *Phys. Rev. B* **1996**, *54*, 11169–11186. [CrossRef] [PubMed]

34. Perdew, J.P.; Burke, K.; Ernzerhof, M. Generalized gradient approximation made simple. *Phys. Rev. Lett.* **1996**, *77*, 3865–3868. [CrossRef] [PubMed]

35. Kresse, G.; Joubert, D. From ultrasoft pseudopotentials to the projector augmented-wave method. *Phys. Rev. B* **1999**, *59*, 1758–1775. [CrossRef]

36. Blöchl, P.E. Projector augmented-wave method. *Phys. Rev. B* **1994**, *50*, 17953–17979. [CrossRef]